Time-resolved temperature characterization of a hypersonic shock layer using a single high-speed color camera for aerospace design applications

Article *in* Measurement Science and Technology · April 2019

DOI: 10.1088/1361-6501/ab1c41

3 authors:

Sneh Deep
Indian Institute of Science

Yedhu Krishna
King Abdullah University of Science and Technology

Jagadeesh Gopalan
Indian Institute of Science

Measurement Science and Technology

Time-resolved temperature characterization of a hypersonic shock layer using a single high-speed color camera for aerospace design applications

To cite this article before publication: Sneh Deep *et al* 2019 *Meas. Sci. Technol.* in press https://doi.org/10.1088/1361-6501/ab1c41

Time-resolved temperature characterization of a hypersonic shock layer using a single high-speed color camera for aerospace design applications

Sneh Deep[a,*], Yedhu Krishna[a], Gopalan Jagadeesh[a]

[a]*Department of Aerospace Engineering, Indian Institute of Science, Bangalore-560012, India*

Two-Color Ratio Pyrometry (TCRP) using a high-speed color camera has been used for temperature characterization of a hypersonic shock layer. The camera, used as a pyrometer, was calibrated in-house using a monochromator, to determine its spectral responsivity and was used to acquire time-resolved images of the flow field over test models at a frame rate of 20,000 fps to understand the evolution of temperature inside the shock region. The optical efficiency of the monochromator and other optical equipment were determined separately and corrected for. Two test models, a flat-faced cylinder of diameter 70 mm and a hemisphere of diameter 80 mm were used for the experiments to study the effect of geometry on the results. Experiments were performed in a Free-Piston Driven Shock Tunnel at a stagnation enthalpy of 5.2 MJ/kg. The average steady state temperature in the stagnation region in case of the cylinder was about 3650 K ± 3% (uncertainty in shock layer due to camera noise) and for the hemisphere it was 3300 K ± 6%. The resolved temperature was 14% higher than that obtained from a similar, but time integrated measurement obtained using a DSLR camera. Steady, 2D numerical simulations were performed to reconstruct the 3D flow assuming azimuthal symmetry and an algorithm was developed to use the shape of the temperature profile along the line-of-sight (LOS) derived from simulations to predict the actual stagnation plane temperature from the experimental LOS-integrated TCRP-derived temperature. The actual temperature in the stagnation region on the vertical plane of symmetry (stagnation plane) for the cylinder and the hemisphere were higher by 2.76% and 1.77% respectively, than the corresponding TCRP-derived LOS integrated temperature. The results are promising for future use in determining intense temperature gradient and heat flux in the vicinity of space vehicles and design of efficient thermal protection system.

1. Introduction

Accurate information on the temperature distribution in the hypersonic shock layer around an aerospace vehicle is an essential design input. Knowledge of temperature can prove vital in the choice of smart materials for designing effective thermal protection systems (TPS) to shield the vehicles from the intense heat flux they encounter while grazing through a planetary atmosphere [1,2]. Experiments are also necessary to validate the numerical simulations of these flows.

Current literature is replete with various methods, both intrusive and non-intrusive, for the measurement of temperature. The most widely applied among intrusive methods is the use of physical instruments like thermocouples or gas-sampling probes [3-7]. These probes have clear-cut disadvantages, such as disturbing the flow, slow response time, susceptibility to damage in harsh environment, limited temperature range and single point measurement. As a consequence, several non-invasive optical methods such as emission spectroscopy [8], and planar laser-induced fluorescence (PLIF) [9,10] have been developed of late to tackle these shortcomings.

A commonplace, inexpensive and non-intrusive temperature measurement technique is infrared thermometry [11,12], where infrared (IR) cameras predict temperature by fitting Planck's curve to the emission obtained from the source in the IR region of the spectrum. However, a pitfall in the technique is that the source emissivity must be known as a prerequisite for accurate measurements, which is hardly a constant and difficult to measure in reacting media [13]. The emissivity estimation problem may be overcome by multi-wavelength (two-color or more) pyrometry, which measures temperature using the ratio of radiant intensities from the source at two or more different wavelengths [14,15]. Though handy, the technique does not yield spatially-resolved temperature in its conventional form. A specific alternative of the ratio pyrometry concept − two-color ratio pyrometry (TCRP) using commercial digital cameras − has acquired prominence recently for spatially-resolved temperature measurements [16-18], owing to simplicity in instrumentation.

Knowing the spatial variation of temperature is of paramount importance, particularly in the shock layer of blunt bodies where the temperatures may shoot from

*Corresponding author
E-mail address: snehdeep@iisc.ac.in

relatively lower values just behind the shock front to extreme values at the stagnation point. Although the TCRP technique had been put into use in a variety of applications involving temperature measurement of radiating solid bodies or soot particles in fuel combustion [16-18], it was never used for shock layer temperature characterization in short-duration facilities until recently. Deep et al. [19] measured the temperature distribution within the radiating shock layer of a cylindrical body with spike using a commercial digital single lens reflex (DSLR) camera as the detector. Experiments were accomplished in a free piston driven shock tunnel, a ground testing impulse facility capable of simulating high-enthalpy hypersonic flow in its test section. Such facilities are marked by extremely short steady test time, of the order of only hundreds of microseconds, within which all the data acquisition must be performed. Application of TCRP in shock tunnel is based on the assumption that the radiating shock layer emits as a gray body over the visible region (~400-700 nm) of the electromagnetic spectrum [20,21], due to the soot/dust particles in the shock tunnel. Gray body is a source of radiation that has uniform emissivity as a function of wavelength. Gray body assumption is common in pyrometric measurements on soot particles, for the wavelength of interest. Previously, attempts have been made to predict the shock layer temperature by fitting Planck's blackbody curve to the emission spectra obtained from the shock layer using fiber-based systems [22,23]. Emission spectroscopy performed in our shock tunnel also confirmed that the shock region majorly radiates as a continuous broadband source. After accounting for spectrometer's instrument broadening, contribution from discrete line emissions due to impurities such as Na and Fe to the overall radiation intensity from the tunnel was found to be negligibly small [19]. As a result, measuring the temperature based on the broadband radiation from the soot particles due to paper and metal diaphragms as well as from the dust particles, assuming the shock layer to be a gray body source, would provide an idea about the conditions prevailing inside the shock tunnel. Even in the presence of uncertainties caused by gray body assumption and minor contribution from line emission, temperatures close to the theoretically predicted values are achieved using TCRP with an experimental configuration much simpler compared to that used in spectroscopic techniques such as planar laser induced fluorescence. This makes TCRP a convenient technique to monitor shock layer conditions, especially near the stagnation region where the temperature is high, and radiation is strong.

However, the temperature measurements performed by Deep et al. [19] using a DSLR single frame camera suffered from time integration of intensity acquired in the shock layer during the entire illuminated period. Temperatures in a shock tunnel are highest during the test time (typically a few millisec) and fall considerably before and after the said period. Integration over a long time will therefore yield a temperature less than the steady period temperature. As mentioned in that paper, the real significance of that work is that it demonstrated the ability of a cheap commercial DSLR camera to identify the contours of high temperature in a shock tunnel. However, accurate time-resolved quantitative measurements in a short-duration facility like shock tunnel would not be possible using it. For that, a high-speed camera is needed.

Also, since TCRP is a line-of-sight technique, the deduced temperature is bound to be sensitive to the unknown spatial distribution of properties along the radiation path length in the viewing direction (line-of-sight). Therefore the measured temperature was 'line-of-sight integrated' also. Various critical physical properties in the hypersonic shock layer; such as surface convective heat flux, degree of viscous interaction between the boundary layer and the outer potential flow, etc. are dependent directly on temperature and it is imperative to measure them as a function of time. This yields an insight into the instant at which these quantities reach a maximum and help in the design process. Also, line-of-sight integrated temperature will be weighed down by low temperatures along the viewing path and will be less than the actual maximum temperature.

The current paper has two major improvements from the above-mentioned work. One is the use of high speed camera, which can yield time-resolved intensity during the steady test time due to its large frame rate provision. This is a major improvement which makes the technique applicable in the shock tunnel. In this study, a high speed camera operated at a large frame rate has been used to acquire time resolved images of the flow field, so as to comprehend the evolution of temperature as a function of time. The instant at which the first glow appears in the test section is taken as the starting time for the evaluation. Since the camera sensor is basically an array of photo-sites called pixels, it yields the radiance (intensity) from the flow, as intercepted by the pixels. In order to relate radiance to temperature, a characterization of the camera was performed. The spectral efficiency of the optical system in the pipeline was determined a priori and corrected for during the camera characterization.

Another important improvement in the current investigation is to perform numerical simulations to see the variation of temperature along the radiation path length, i.e., along the line-of-sight. This was not performed by Deep et al. [19] and hence the 2D temperature obtained based on the path-integrated signal of a flow which is essentially 3D in nature was assumed to be the actual temperature, and the effect of non-uniform distribution was not corrected. In the current paper, the shape of the temperature profile inside the shock layer along the line-of-sight was interpreted by means of a numerical model of the flow field developed in Ansys Fluent 14.5, based on the

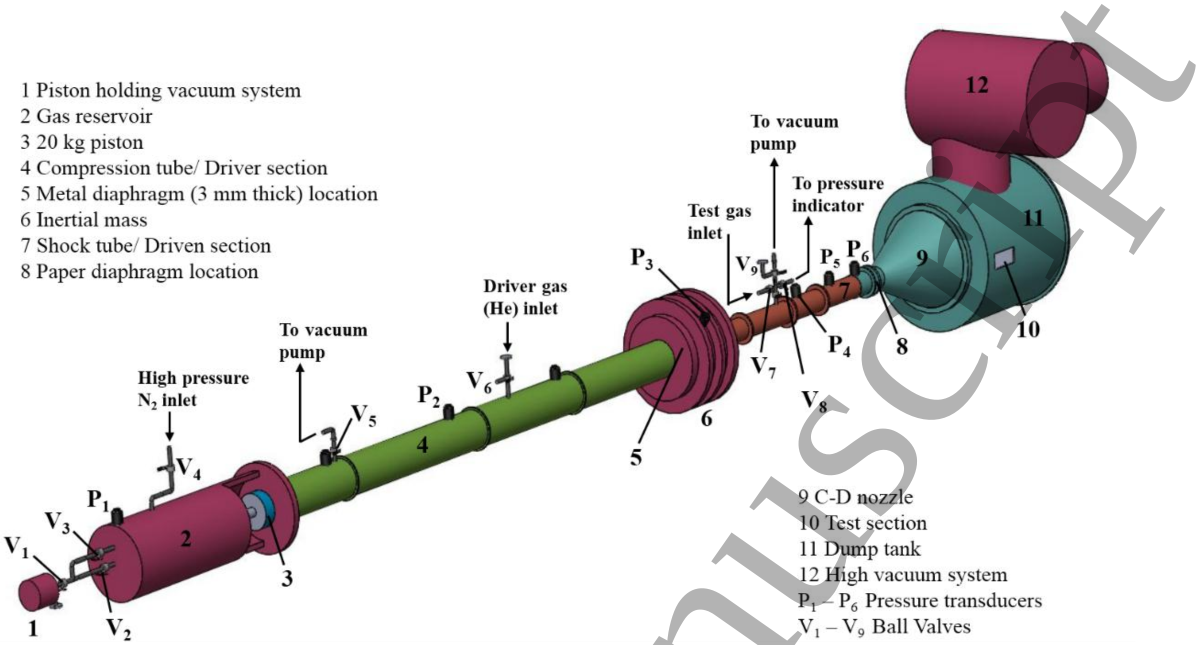

Fig. 1. A detailed schematic of the HST3 free-piston driven shock tunnel with various parts labelled. The control valves and pressure transducers have also been marked.

Reynolds-averaged-Navier-Stokes (RANS) equations. Detailed complementary CFD simulations thus provided a physical description of the three-dimensional flow field and a subsequent algorithm developed by us helped obtain the actual maximum shock layer temperature from the 'integrated' temperature derived from TCRP. Besides, calculations are also influenced by a large number of uncertainties creeping up from the measurement principle, test conditions and the experimental set up [24]. An analysis of the measurement uncertainties is also provided. The experiments were conducted in the free-piston driven shock tunnel (FPST) HST3, housed at the Laboratory for Hypersonic and Shock Wave Research (LHSR), Indian Institute of Science (IISc). Details of the work outlined in this paragraph are furnished in devoted sections that follow, together with the results and discussion.

2. Experimental facility

2.1. The free-piston driven shock tunnel (FPST)

The free-piston shock tunnel (FPST), conceptualized by Stalker [25], is regarded as one of the most suitable ground testing facilities for hypersonic, high enthalpy flow research of re-entry vehicles. Our experiments were conducted in an in-house FPST, capable of simulating stagnation enthalpies of up to about 25 MJ/kg, so as to allow efficient study of gas dissociation effects also.

A detailed schematic of the FPST, with all its major parts labelled, is shown in Fig. 1. It is an 'impulse' facility, producing extremely small test times (of the order of hundreds of microseconds) in its test section. The heavy piston initially stationed at the reservoir-compression tube junction acts as the compression device of the driver gas filled in the tube at a low pressure. The reservoir is filled with high pressure nitrogen and the piston is released. It accelerates down the tube until it ruptures a metal diaphragm separating the compression tube and the shock tube. At this point, a primary shock wave travels through the test gas in the shock tube and reflects at the paper diaphragm, bringing the test gas behind it to rest and elevating its temperature and pressure many-fold. The gas then expands through the converging-diverging (*De Laval*) nozzle, attaining hypersonic velocities and producing the required conditions in the shock layer of the model placed in its test section. For a detailed account of the dimensions of the various parts of the HST3 shock tunnel, their functioning, the role of various valves (V) and pressure transducers (P) and the nitty-gritty of the tunnel operation, the reader is referred to the doctoral dissertation of Jayaram [26] and Chintoo [27].

2.2. Shock tube measurements

The compression tube is purged and filled with the driver gas, helium, to a pressure of 700 mm of Hg (0.093 MPa). Depending on our intended final conditions in the test section, the shock tube was filled with the test gas, atmospheric air, to 230 mm of Hg (0.0306 MPa). Near-vacuum conditions are maintained in the dump tank so as to ensure that the nozzle operates in the third critical mode (design operation) up to its exit plane, where hypersonic flow is achieved [28]. Next, the piston is fired at a judicious pressure of N_2 from the reservoir, so as to ensure its soft landing [29], and thus, minimize damage to the other end of the compression tube. As the driver gas is compressed, the Al diaphragm bursts at a pressure of 10 MPa, as measured by the P_3 sensor. The speed of the primary normal shock travelling down the tube was measured to be 2364 m/sec (Mach 6.8) by monitoring the time difference between pressure jumps recorded by the P_4, P_5 and P_6 transducers separated by a known distance. The stagnation pressure behind the reflected shock, as measured by P_6, was 8.88 MPa. The stagnation temperature and enthalpy were inferred from a specialized numerical code called STN [30] that takes 'real gas' effects into account. They were 3643 K and 5.2 MJ/kg respectively.

2.3. Test models

Two different test models readily available were used for the experiments, to examine the effect of geometry and temperature profile along the line-of-sight on the relation between the TCRP-derived integrated temperature and actual temperature. A hemispherical model, with a diameter of 80 mm and a flat-faced cylinder with a diameter of 70 mm and a length of 120 mm were subjected to identical experimental conditions separately. A photograph of the models is shown in Fig. 2, with the free stream direction marked.

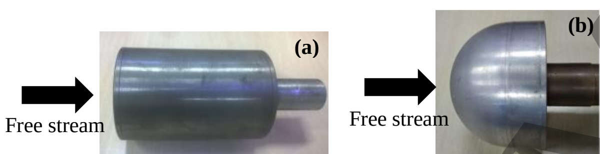

Fig. 2. Photograph of the test models. (a) Flat-faced cylinder and (b) Hemisphere. The direction of the free stream has been marked by a black arrow.

3. Experimental technique and set-up

3.1. Two-color ratio pyrometry (TCRP) fundamentals

TCRP makes use of the ratio of signals in two color channels of a color camera to estimate the temperature, assuming that the light source is a gray body. High speed color cameras possess either a CCD or a complementary metal oxide semiconductor (CMOS) sensor positioned behind an RGB (red, green and blue channel) color filter array (CFA). When the sensor receives intensity from the source, it produces a signal S given by Eq. (1):

$$S_i = \int_{400nm}^{700nm} \int_{\varphi} \int_{A} \tau_i(\lambda)\, I(\lambda, T) dA\, d\varphi\, d\lambda \quad (1)$$

where i represents one of the R, G or B color channels, τ is the combined spectral responsivity of the CFA and the gain of the internal electronics of the detector, I is the spectral radiance from the source and the environment within the optical path, A is the area of the flow field within the field of view of the detector, φ is the solid angle subtended by the detector and λ is the wavelength with limits 400 nm and 700 nm as decided by the responsivity of the camera. Since the sensor area is much smaller than its distance from the flow field, and the sensor has a high spatial resolution, it may be proved [24] that the above equation may be expressed in a simplified form as Eq. (2):

$$S_i = C(A, \varphi) \int_{400nm}^{700nm} \tau_i(\lambda)\, I(\lambda, T)\, d\lambda \quad (2)$$

where C is a constant that takes into account the original variables A and φ.

The spectral radiance per unit wavelength, I from a gray body is given by the Planck's law as in Eq. (3):

$$I(\lambda, T) = \varepsilon \frac{2hc^2}{\lambda^5(\exp(hc/\lambda kT)) - 1)} \quad (3)$$

where ε is the emissivity of the source, h is the Planck's constant, k is the Boltzmann constant, c is the speed of light, λ is the wavelength and T is the temperature of the source. Now, since it is cumbersome to determine the constant C in Eq. (2) and source emissivity ε, TCRP comes into the picture with an ingenious solution of taking a ratio of detector signals for two different channels i_1 and i_2 to yield Eq. (4):

$$\frac{S_{i_1}}{S_{i_2}} = \frac{\int_{400nm}^{700nm} \tau_{i_1}(\lambda) I(\lambda, T)\, d\lambda}{\int_{400nm}^{700nm} \tau_{i_2}(\lambda) I(\lambda, T)\, d\lambda} \quad (4)$$

It is to be noted that the constant C, being independent of the color channel is cancelled in the ratio. Likewise, based on the grey body assumption, ε also gets cancelled. Hence, the experimentalist is spared of an added task of calculating these two quantities separately. The ratio can be readily ascertained for a range of temperatures by evaluating the integrals in Eq. (4) numerically after determining the spectral characteristics τ of the camera system. This is done by characterizing the high speed camera against a source of known spectral radiance.

3.2. Camera characterization

The optical set-up used in this work for camera characterization has been shown in Fig. 3. Table 1 lists the specifications of the optical components. Continuous broadband light from a calibration lamp of known spectral radiance was made to pass through a monochromator to obtain a single wavelength with a resolution of 0.1 nm at its exit slit. This light was imaged onto a high speed color camera through a Nikkor objective lens. The camera was externally controlled on a computer by the PCC software provided by the manufacturer. The BK-7 optical window of the shock tunnel was also a part of the set-up so as to take into account its transmissivity during the calibration, as light from the shock layer in the test section passes through the same window during actual experimentation. The quantum efficiency of the monochromator (not provided by the manufacturer) was ascertained in a separate experiment using a photodetector of known spectral response positioned at the monochromator exit.

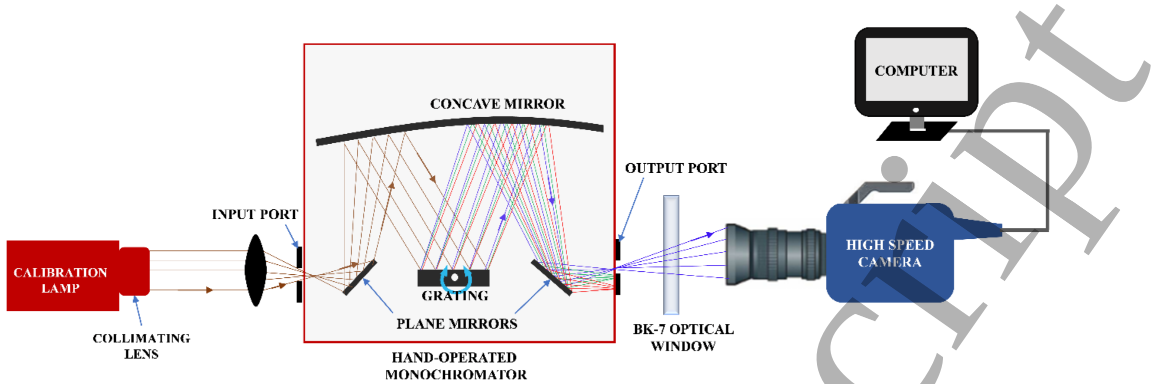

Fig. 3. A schematic of the optical set-up for high speed camera characterization. A ray is traced from the calibration lamp to the high speed camera by arrows.

Table 1
Technical specifications of the optical components in the set-up.

Component	Specifications
Calibration lamp (Thorlabs SLS201/M)	Stabilized tungsten- halogen light source, Spectrum: 300-2600 nm, includes uncoated aspheric condenser collimating lens (SLSC1)
Hand-operated monochromator (Newport 77250-MC)	77298 grating assembly, Ebert-Fastie design, ruled with 1200 lines/ mm, 360 nm blaze, Spectrum: 200-1000 nm, Least count: 1 nm, Resolution: 0.1 nm
High speed color camera (Vision Research Phantom v310)	Sensor: CMOS, Pixel resolution: 1280 x 800, Bit-depth: 8-bit and 12-bit, Max. frame rate: 500000 fps, Spectrum: 400-700 nm for color images, Objective: Nikkor AF-D, 80-200 mm, f/2.8
Photodetector (Newport 818-BB-27) -not shown in set-up	Silicon biased, 2.55 mm active diameter, 3 ns rise time, Spectrum: 200-1100 nm

The calibration lamp was left switched on for about 10 minutes to obtain a stable output. The collimated beam was passed through a monochromator, manually adjusted from 400-700 nm in steps of 10 nm and the dispersed beam egressing from the exit slit was imaged on to the camera's detector. Three such TIFF images have been shown in Fig. 4. It is imperative to avoid the camera's built-in post-processing algorithms and record images in the 'raw' mode also, so as to obtain the original, unadulterated source intensity information. Videos of the monochromatic beam were acquired in the raw file format (*.cine) and a total of 51 images were segregated and saved in a MATLAB readable format. An average intensity was obtained from these images to account for any time variation of lamp intensity, however small. An optimum exposure of 1250 μsec was used to obtain unsaturated intensities in each of the R, G, and B color channels. As evident from Fig. 4, the spatial distribution of intensity was non-uniform in the illuminated region and hence an array of 100 (10×10) pixels in the center was used for average intensity computation. After procuring time and space averaged RGB intensities at sampled wavelengths, they were corrected accounting for monochromator efficiency and then divided by the source's known radiance to discern the spectral responsivity (τ) of the CFA for each color channel. Since the camera optics is sensitive only in the visible region of the spectrum (~ 400-700 nm), all measurements were confined to that region. The spectral responsivity of each color channel is shown in Fig. 5. The responsivity is normalized in the range 0-1. Next, Planck's spectral radiance for a range of temperatures was simulated and multiplied by the spectral responsivity of the CFA. Using the simulated camera response curves thus obtained, the area under them was determined and ratio calculated.

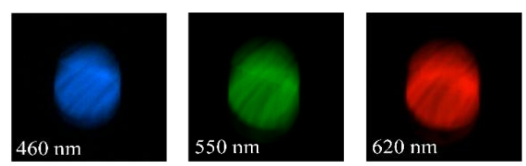

Fig. 4. Calibration images at three chosen wavelengths.

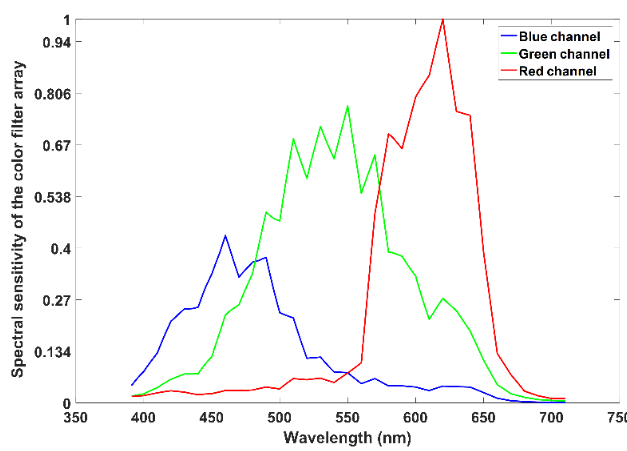

Fig. 5. Normalized spectral sensitivity of the color filter array for each color channel.

Since there are three color channels, an equivalent number of ratios were obtained: R/G, G/B and R/B for each temperature. The procedure ultimately yields a look up table of temperature vs. signal ratio in which the latter is single valued over the temperature range of interest.

Experiments in the tunnel yielded saturated signals in the R channel for some pixels. Hence, the G/B ratio was used for TCRP. Also, for temperature range expected in the experiments, G/B provides better sensitivity to temperature variations. Fig. 6 shows the obtained characterization curve. The apparatus is sensitive enough to changes in temperature up to about 7500 K, after which the G/B ratio becomes almost asymptotic to the abscissa and it becomes difficult for the technique to yield precise temperature values for a signal ratio.

Since the TCRP technique is based on a ratio of signals from two different color channels, any non-linearity in the CMOS sensor output will affect the temperature. The linearity of the CMOS chip was also characterized as a part of this work using the calibration lamp. The simple linear regression model was used to obtain the best fit line for the scattered data in the G and B colour channels. The coefficient of determination (R^2), indicating the quality of the fit was calculated to be 0.9951 and 0.9993 in the G and B channels respectively. The values are very close to 1, indicating an excellent linearity between camera signal and radiant intensity. Since the sensor exhibits linearity, the temperature results will be unaffected.

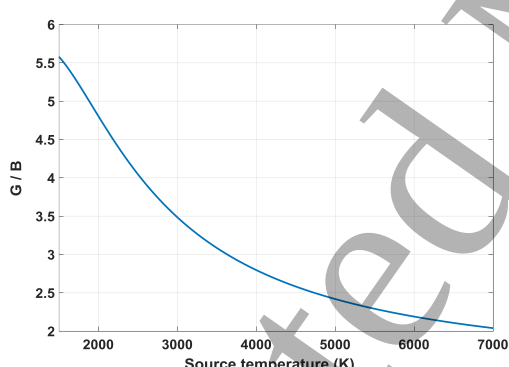

Fig. 6. Camera characterization curve of G/B vs temperature.

3.3. TCRP Algorithm

The TCRP algorithm, comprising of a series of steps that lead to a 2D temperature contour starting at the raw intensity video acquired from the experiment, is explained in brief. First, a video of the flow was acquired by fixing the camera on a tripod stand outside the test section window and focusing it on the model in the test section in a direction perpendicular to its axis. All post-processing options were disabled, and a raw *.cine video was procured. The camera was operated at a large frame rate to record a time resolved flow. To reduce the file size and the external image processing time, the resolution was maintained just enough to image the entire shock layer formed. The raw video was next separated into its constituent images, saved as *.dng files and read into MATLAB. A baseline (dark) image was procured at the same exposure and deducted from the raw image to get rid of the background noise. The final raw image was a gray-scale one, with a single intensity value at each pixel. It was converted into a full color image, with a bit-depth of 12 in each channel, by a demosaicing technique [31] to obtain R, G and B intensities at each pixel. Next, G/B signal ratio was obtained on a pixel-by-pixel basis and mapped to a temperature contour using the calibration curve in Fig. 6. The steps were repeated for each image. It is to be borne in mind that the obtained contours are 'integrated' values along the line-of-sight.

3.4. Shock tunnel experimental configuration

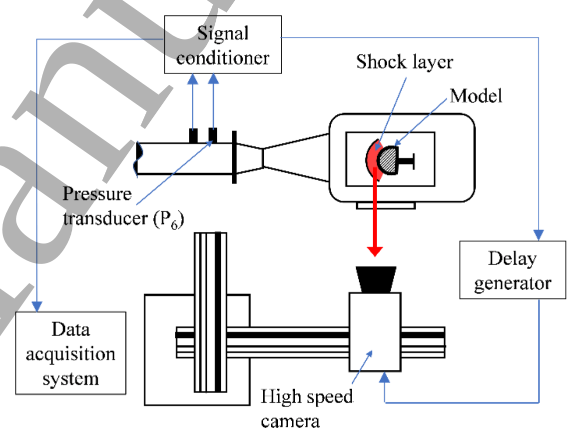

Fig. 7. Schematic of the shock tunnel configuration and data acquisition system, together with the high speed camera.

To acquire a video of the hypersonic flow during the experiments, the camera was placed at a distance of about ~2 m from the test model and focal length of the lens set to 80 mm for a sharp image so that the entire model and the shock layer in front of it is covered and a good signal level is achieved on the pixel covering the shock region. No hardware binning was possible since the camera was a CMOS camera. No software binning was conducted since the spatial resolution was low. Video was acquired at a large frame rate of 20,000 fps, with each frame covering a duration of 50 µsec. For the required frame rate of 20000 fps, the spatial resolution of the images was only about 0.56 mm/pixel. Fig. 7 is a schematic of the experimental configuration. An exposure of 49 µsec was maintained. Although for this exposure, the red channel in some pixels was found to be saturated, the green and blue channels provided a good signal-to-noise ratio (SNR) due to high temperatures in the shock layer, and as such the G/B ratio was used for temperature characterization.

A frame duration of 50 µsec was chosen after a few trials. Higher values would lead to saturation of the color channels and lower values would give poor signal levels. Moreover, the steady-state flow duration of the shock tunnel was only about 260 µsec. Therefore, 50 µsec was sufficient to freeze the dynamics of the measurement scene, as confirmed from Table 4 in the manuscript. After the attainment of steady time at 300 µsec, the temperatures measured at intervals of 50 µsec are almost constant and vary within uncertainty limits of the apparatus. This suggests that within the steady test time, in spite of the turbulence levels, the temperature is relatively constant.

Videos were captured in a proprietary raw format, *.cine, so as to prevent all internal processing and let the experimentalist have full control over the post-processing. Individual frames were then extracted from the raw video, both as *.dng files (for analysis in MATLAB) and *.jpg files (for presentation purpose).

3.5. Correction for the effect of non-uniform temperature distribution along the line-of-sight

Like any line-of-sight (LOS) optical technique, TCRP presumes invariant temperature along the radiation path length. This is however far from reality in a shock layer, where temperature gradients are rampant throughout its structure [32]. Such non-uniformities can adversely affect the TCRP measurements. The present work is a step towards interpretation of TCRP integrated temperature and studying its sensitivity to temperature distribution along the LOS, thereby estimating the actual temperature at the stagnation (central) plane location in the shock layer. The approach starts with an axisymmetric, 2D shock layer temperature distribution $T(x,r)$ simulated by means of a numerical model developed in Ansys Fluent 14.5 CFD software. The following subsections elucidate the numerical model and its manipulation to establish a relationship between the stagnation plane temperature and the TCRP-derived one.

3.5.1. Numerical model

Separate simulations were performed for the cylindrical and hemispherical test models. 2D, axisymmetric geometry was generated to save computational time and the flow field was captured with about 300,000 cells after a grid-independent study. The computational volume was made large enough in order to negate the boundary effects. The governing equations, namely the mass conservation, Reynolds-averaged momentum conservation (Navier-Stokes for turbulent model) and energy equation were discretized using the cell centered finite volume approach. A density-based, steady state solver was used, with the former accounting for compressibility effects that become conspicuous in hypersonic flow. The free stream Reynolds number was 5.8×10^{5} per unit length, implying a turbulent flow. Therefore, the two-equation k-ω SST turbulence model, known to augment the fidelity of computations in chemically reacting flow [33,34] was employed, with the species transport model incorporated to simulate the chemical reactions in the shock layer. Thorough finite-rate chemistry was setup for external hypersonic flow. The Eddy Dissipation Concept (EDC) model was applied to predict the turbulence-chemistry interaction. Air was taken as the test gas, consistent with experiments, with mixing law formulation for isobaric specific heat (C_p), thermal conductivity (k) and viscosity (μ) of the bulk gas. A 5-species (NO, N, O, O_2 and N_2), 5-reaction (volumetric type) model was used for the computations, sufficient for our case where no ionization of gases is expected. The modeled reactions are listed in Table 2.

Table 2
5-reaction model used for the finite rate chemistry.

Reaction Name	Reaction
O_2 dissociation	$O_2 = 2O$
N_2 dissociation	$N_2 = 2N$
NO dissociation	$NO = N + O$
N_2-O exchange	$N_2 + O = NO + N$
NO-O exchange	$NO + O = N + O_2$

Piecewise linear C_p with temperature variation obtained from NASA polynomials look up table [35], kinetic-theory based k, and Sutherland law based μ were input for each species. The temperature-dependent forward rate constant for each reaction was predicted by the modified Arrhenius rate equation [36]. The equation requires several inputs such as a pre-exponential factor, temperature exponent, reaction activation energy and the universal gas constant. The first three are reaction dependent and are obtained from the NIST database [37]. Next, suitable boundary conditions (BCs) were allocated to the flow domain. Stationary wall with no-slip, isothermal and zero species diffusive flux BCs were specified at the wall. Pressure-outlet and pressure-far-field BCs were specified at the outlet and inlet boundary respectively. The line of rotational symmetry has been specified as the axis. The flow field is initialized with the free stream (far field) conditions. An absolute convergence criterion was used, and the simulation was run until all the residuals fell to at least 1×10^{-06}. The modeled domain along with the BCs, for the cylinder and hemisphere has been shown in Fig. 8.

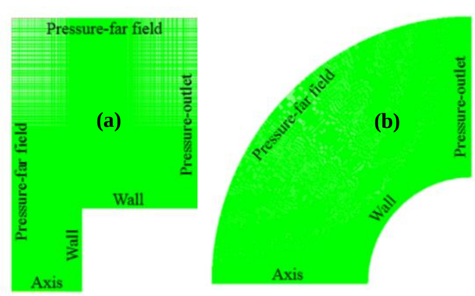

Fig. 8. Modeled domain with BCs. (a) Cylinder and (b) Hemisphere.

3.5.2. Relation between stagnation-plane temperature and TCRP temperature

The converged numerical simulation yields a 2D distribution of physical quantities in the shock layer. Since both the models possess cylindrical symmetry, the quantities are invariant in an ideal flow in the azimuthal direction ($\frac{\partial()}{\partial\theta} = 0$). The 2D solution may thus be rotated about the axis to yield a full 3D distribution. Radiation propagation inside the shock occurs through emission and absorption, which together determine the amount of radiation intercepted by the camera. Following are the assumptions made: (a) Radiation propagates along lines parallel to the shock symmetry plane; (b) The shock layer is an amalgamation of several tiny pockets of gas layers with soot particles, each behaving as a grey body and emitting a spectral radiance depending on its temperature based on Planck's law and weighted with the corresponding density fraction, as in Eq. (5):

$$I_{camera}(\lambda, T_{int}) = \sum_{i=1}^{n} I_{shock\ layer}(\lambda, T_i) * \rho_i/\rho_{max} \quad (5)$$

where I_{camera} is the net intensity as would be received by camera, $I_{shock\ layer}$ is the Planck's intensity leaving the ith pocket in the modeled shock layer whose temperature is T_i and density is ρ_i and ρ_{max} is the maximum density along the line-of-sight. T_{int} is the temperature corresponding to the integrated signal on the camera I_{camera}. i spans across the line of sight, taking all points along the LOS (divided into n points). Fig. 9 is a schematic showing the propagation of radiation along the line of sight.

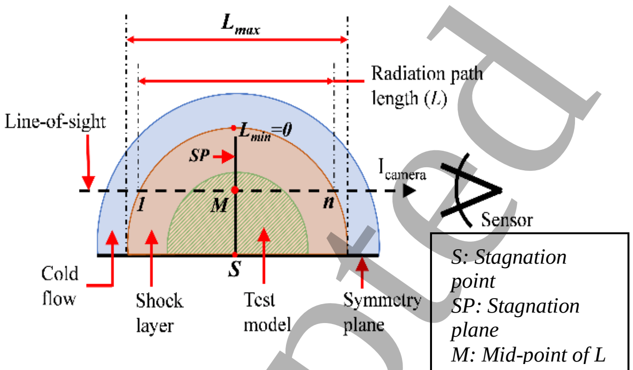

The free stream direction is into the plane of the paper

Fig. 9. Schematic of propagation of radiation along line-of-sight. Path length (same as shock thickness) varies from zero to L_{max}.

Reabsorption of signal has not been taken into account in this work in Eq. (5). Since the total intensity falling on the camera is decided by the product of the emitted radiation and the absorptivity, it won't affect the temperature results from TCRP due to the grey-body assumption. The absorptivity, just like emissivity, would be independent of wavelength due to this assumption and would get cancelled out while calculating the color channel ratio. Even without grey body assumption, the effect has been shown to be small (typically ~1%) [38]. So the effect of reabsorption is neglected in this work.

T_i was known from the simulation at all points, $1\ to\ n$, along any chosen line-of-sight. Hence, $I_{shock\ layer}$ was computed at those points from the Planck's law. Since ρ_i and ρ_{max} on the LOS were also known, Eq. (5) was used to determine the net radiation I_{camera} viewed by the camera. This radiation is a spectrum that spans over the visible region. By normalizing it with the maximum value and iteratively fitting it with the normalized Planck's equation by the method of least squares, the corresponding temperature T_{int} was obtained. The algorithm was repeated for all LOSs covering the volume of the shock layer, thereby securing a 2D distribution of the integrated temperature. This would be the expected TCRP-derived temperature, if the actual temperature profile were to be the same as that given by simulation. MATLAB was used for all coding purposes.

Next, the 2D distribution of integrated temperature from simulation was compared to that obtained by TCRP from the actual experiments in the tunnel. Although the shape of the temperature iso-lines were quite similar in both the cases; the absolute values were disparate. At any point, the TCRP calculated temperature was lower than its simulation-derived counterpart. A possible cause is losses in the shock tunnel flow. The actual flow in the nozzle experiences wall friction and heat loss to the conducting walls, which have been neglected. The enthalpy assumed may not be achieved in reality due to these losses.

The following iterative algorithm was adopted to predict the actual temperature in the stagnation plane using the simulation result and experimental data. It was assumed that the shape of the unknown profile in the experiment was the same as that in the simulation. Every LOS in the simulation has a temperature midway of the radiation path length, i. e., at the intersection of the LOS and the vertical stagnation plane (called so as it contains the stagnation point S), marked M in Fig. 9. Let it be called T_{mid}. Different values of T_{mid} were taken and the entire temperature profile was successively scaled with a factor equal to the ratio of the original T_{mid} and the new value $(T_{mid})_{new}$. For each scaled profile, an integrated temperature was obtained following the procedure outlined in the previous paragraph. The profile, for which the integrated temperature matched that from experiment, was fixed as the actual experimental temperature profile and the corresponding $(T_{mid})_{new}$ was fixed as the actual temperature on the stagnation plane. When repeated for all LOSs, a 2D distribution of actual mid-plane temperature was obtained. The rationale behind choosing T_{mid} was that along any LOS, that would ideally be the maximum temperature as it lies on the stagnation plane and any design based on it would be a safe one. In this way, the actual temperature distribution on the stagnation plane was estimated from the TCRP-derived temperature distribution. Since only the profile shape of the temperature distribution along the LOS is used from the simulation instead of the absolute values, the effect of small uncertainties in simulations on the final temperature values are negligible. The results have been reported for both the geometries, to appreciate geometry-based differences.

4. Results and discussion

4.1. Free stream conditions

Pressure transducer (P_5 *and* P_6) signals from the shock tube have been shown in Fig. 10, along with the pressure signal from the pitot transducer mounted in the test section. The signal is amplified for easy visualization. It reveals a steady test time of about 260 μsec, highlighted in light grey. From the pressure and shock speed measurements, another code STUBE 2.5, a 1D code for simulating shock tube nozzle flow, was used to predict the nozzle exit free stream conditions, denoted by a suffix ∞. The stagnation conditions behind the reflected shock, which are also inputs to STUBE, were predicted by STN as mentioned in Section 2.2. Table 3 lists the free stream conditions.

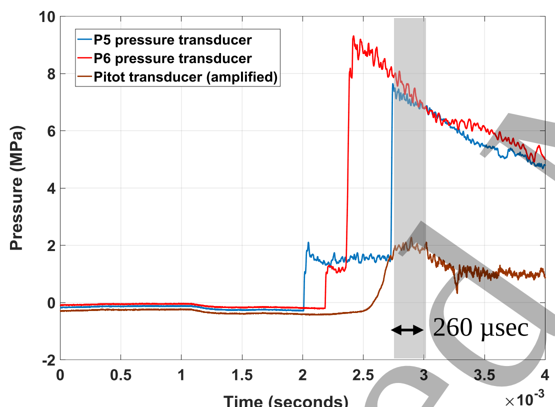

Fig. 10. Shock tube and pitot pressure transducer signals.

Table 3
Nozzle exit free stream conditions from STUBE.

Mach number M_∞	10.06
Static pressure P_∞ (Pa)	210.933
Static temperature T_∞ (K)	246.12
Static density ρ_∞ (kg/m^3)	0.002964
Velocity U_∞ (m/sec)	3072.26
Reynolds number Re_∞ (million/m)	0.58

4.2. TCRP of color images of the flow from the test section to determine temperature evolution with time

Duration of 50 μsec for each frame allowed us to obtain at least four frames in the available flow steady time. The instant at which the first faint glow appears is taken as the beginning of time ($t = 0$ μsec). Fig. 11 shows the *.jpg images of the development of the shock layer over the cylinder and the hemisphere. It was found that just after the steady flow time, the shock layer was disturbed by the paper particles from the paper diaphragm that make their way into the test section and burn in the shock layer. This alters both its structure and temperature. Hence, analysis was confined only to images up to the steady test time.

The images shown in Fig. 11 were read into MATLAB one by one. A dark, baseline image acquired at the same exposure was subtracted from each image to remove stray background intensity falling on the sensor. Unlike most CFAs which possess a Bayer 'RGGB' alignment pattern [39], the v310 camera CFA has a 'GBRG' pattern. This information was used to perform an interpolation step called demosaicing in MATLAB, which converts raw grey intensity image into a full color RGB image. The RGB intensities are thus obtained on each pixel, as arbitrary 'counts'. The color image was next cropped to a region of interest covering the shock layer and a small portion of the model. The G/B ratio was procured at each pixel and mapped to a temperature based on the look up table obtained from camera characterization. Finally, we have a line-of-sight integrated 2D temperature profile. Since a profile is obtained for each time resolved image, a variation of temperature with time may be known. We were mainly concerned with temperature in the stagnation region of the model, as it is the basis of most contemporary design. Since it was difficult to locate a single stagnation point, a small rectangular region of 15 pixels was used to compute an average stagnation temperature. Table 4 gives the relevant numbers.

Table 4
Temperature variation with time.

Image no.	Time (μsec)	Cylinder temperature (K)	Hemisphere temperature (K)
1	0	-	-
2	50	-	-
3	100	3019	2759
4	150	3143	3176
5	200	3096	2815
6	250	3019	2711
7	300	3590	3283
8	350	3597	3309
9	400	3691	3273
10	450	3676	3313

Temperature for the first two frames could not be determined due to an extremely poor SNR. The table reveals important insight into the flow development. From the instant the flow just reaches the model ($t = 0$), the temperature hovers around 3000 K for the cylinder and

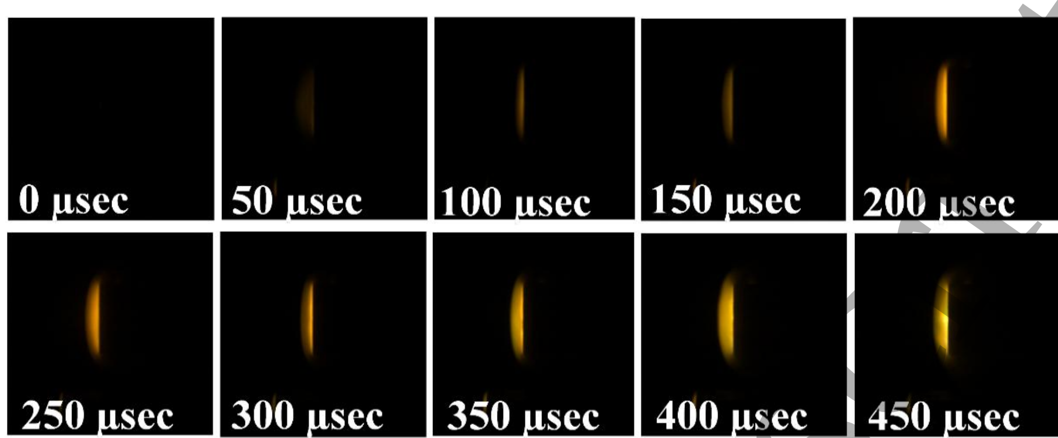

(a)

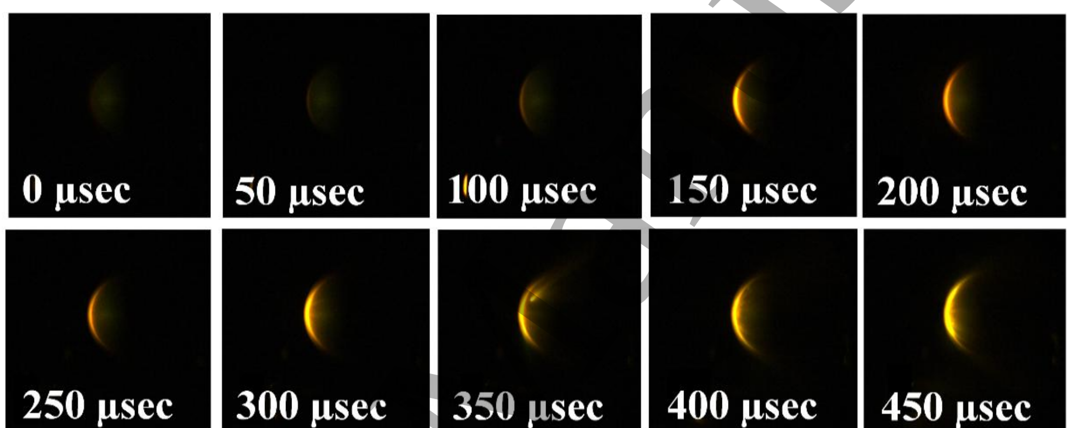

(b)

Fig. 11. Time resolved images of hypersonic, high-enthalpy flow over (a) Flat cylinder and (b) Hemisphere. Each frame covers an interval of 50 µsec. In both the cases, the shock layer was disturbed by paper particles after 450 µsec.

around 2750 K for the hemisphere (except an outlier of 3176 K), for the first 250 µsec. From the seventh image onwards, there is a sudden jump in temperature, remaining almost unchanged thereafter, suggesting onset of steady test time. Since the flow is disturbed after 450 µsec, it is not possible to predict the exact steady test time from the table. But it is certainly greater than 200 µsec. This is in good agreement with the pitot signal in Fig. 10. The signal starts rising, indicating flow arrival, at about 2500 µsec and becomes steady after 250 µsec at about 2750 µsec. It then remains steady for about 260 µsec. TCRP-derived temperature contour at 400 µsec has been shown for both the models in Fig. 12. Location of the model has also been shown along with the 2D temperature map.

The only drawback of the current system compared to the DSLR-based system is the poor spatial resolution for the exposure time settings (49 µs) used in the current experiment. This is the cause for the large and unsmooth pixel-to-pixel variation in the uncertainty. The temperature in the region of interest, i.e., in the shock layer lied between about 2000 K and 4200 K for the cylinder and the hemisphere. The temperature scales have been adjusted to show this variation. The stagnation region utilized for average temperature calculation has been enclosed in a white rectangle. Average stagnation temperature in the selected rectangular region for cylinder and hemisphere are 3691 K and 3273 K respectively.

Emission spectroscopy was performed in the test section of the FPST [19]. Over and above the continuous broadband, sharp emission peaks occur at around 590 nm due to presence of metal impurities like sodium that sweep along with the flow into the test section. Another line due to O atom exists at 777 nm, but was not considered in the present study since it is outside the visible region of the spectrum. These peaks will definitely lead to a cross talk in the color channels and need to be accounted for to obtain a corrected temperature. The procedure for correcting the temperature has been described in Deep et al. [19]. The line corrected temperature is about 78 K higher than that obtained with the line contribution at an absolute temperature value of about 3125 K, and 62 K higher at an absolute temperature of about 2641 K.

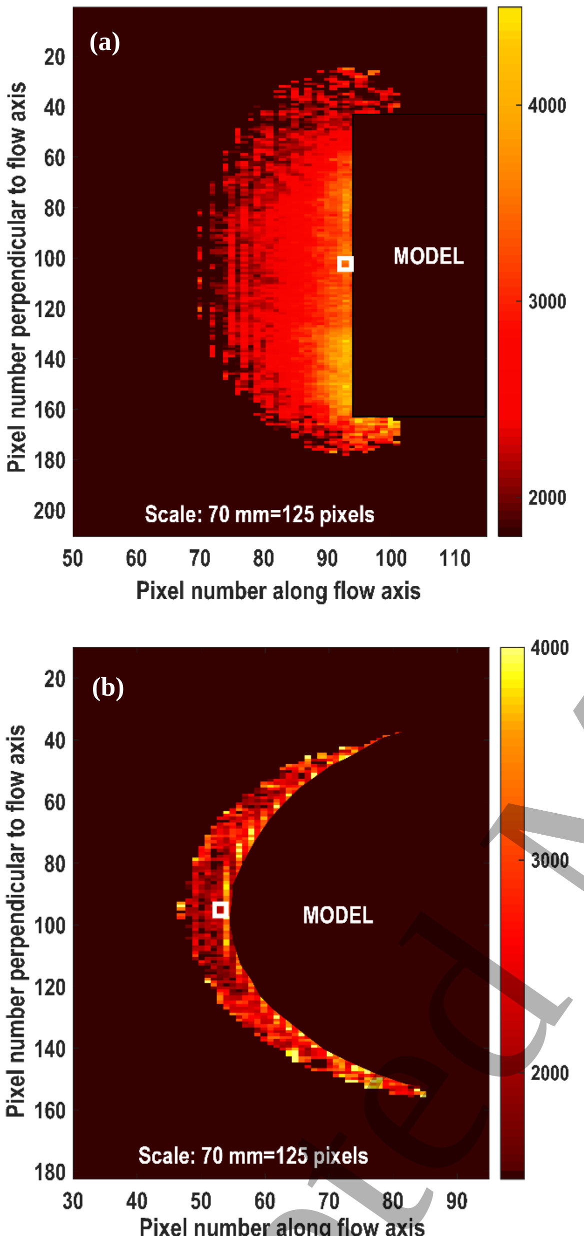

Fig. 12. Illustration of line-of-sight integrated 2D temperature field in the shock layer at 400 μsec over the (a) Cylinder and (b) Hemisphere.

4.3. Comparison of temperature results from the single-frame DSLR camera and the high-speed camera for the cylinder

A comparison of the temperature obtained from the single-frame DSLR camera and from the high-speed camera operated at 20,000 fps (each frame covering 50 μs) has been shown for the cylindrical model in Fig. 13. The time-integrated 2D temperature distribution in the shock layer obtained from the DSLR camera has been shown in Fig. 13(a). The temperature obtained in the stagnation region was about 3237 K, with a run-to-run variation of ± 41 K. The temperature obtained from the high-speed camera during precisely the steady test time at t=400 μsec, as shown in Fig. 13(b), is 3691 K. This is within uncertainty limits of the value of 3643 K predicted by the STN code. Hence, time resolved temperature measurement during the test time shows that the stagnation temperature obtained using the high speed camera is higher by as much as 14% from its integrated counterpart using the DSLR camera. Although the DSLR camera yields a highly spatially resolved temperature distribution in the shock layer, it suffers from the drawback of time integration and hence yields a much lower temperature than expected.

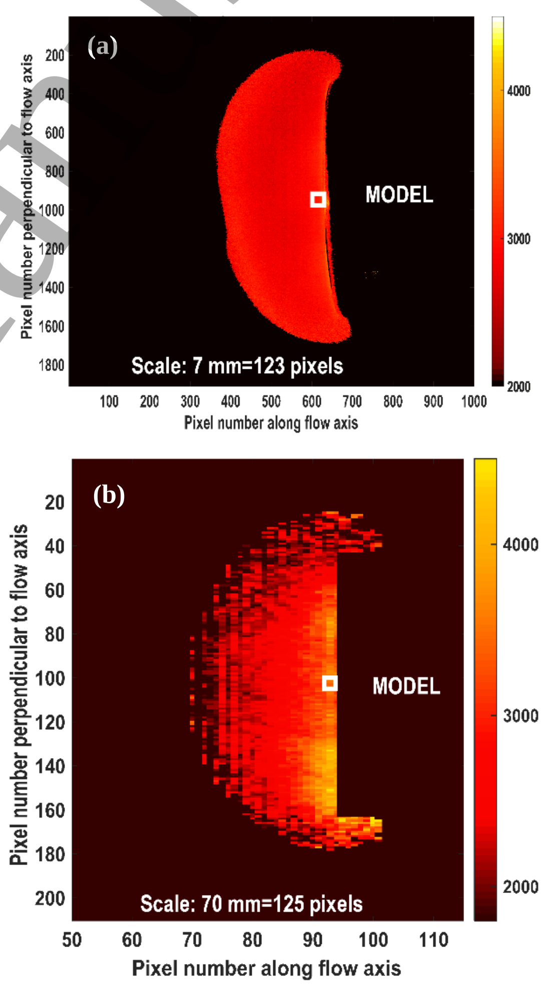

Fig. 13. Comparison of 2D temperature contours obtained from (a) The single-frame DSLR camera and (b) The high-speed camera. The DSLR camera yields a stagnation region time integrated temperature of about 3237 K, whereas the high speed camera gives a value of 3691 K at an instant during the steady test time.

4.4. Temperature contours from Fluent and comparison between stagnation-plane temperature and integrated temperature contours

The nozzle exit free stream conditions obtained from STUBE (in Table 3) were used as far field BCs for the numerical simulations. A pressure of absolute zero was maintained at the pressure outlet to simulate the vacuum condition in the dump tank. The solution files obtained from Fluent were exported into MATLAB as matrices and the 2D contours were plotted. The contour plots of temperature for the cylindrical and hemispherical model have been shown in Fig. 14 for a selected region of the flow field. It is worthwhile to mention that these are the temperature contours on the stagnation plane. Due to circumferential symmetry, if this plane be rotated by 360º about the axis, the full 3D contours would be obtained.

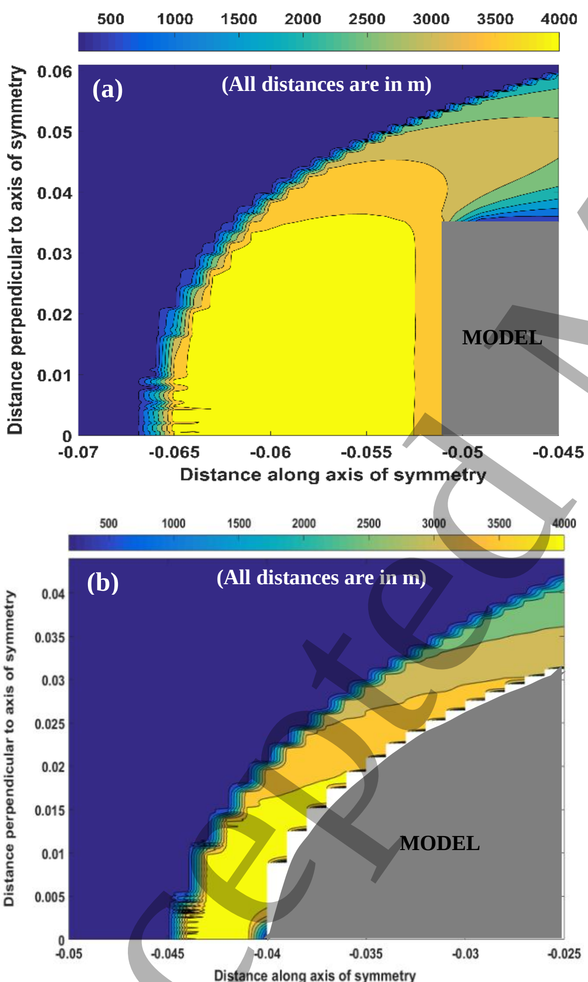

Fig. 14. Temperature contours obtained from simulations on the stagnation plane for flow over the (a) Cylinder and (b) Hemisphere. The models have also been sketched.

Ideally, the maximum temperature location is the stagnation point (on the axis of rotational symmetry) on the model wall, but due to an isothermal wall BC in Fluent, the temperature at the wall remains equal to the room temperature of 300 K (therefore, no inference should be made from that region) and the maximum occurs slightly upstream, where the wall effects become negligible. As one moves away towards the aft of the model, the temperature falls. The maximum temperature in case of the cylinder was about 4290 K at -0.057 m (stagnation point= -0.051 m), while for the hemisphere it was about 4290 K at -0.042 m (stagnation point= -0.04 m) on the axis.

Next, the integrated 2D temperature profile, as would be obtained from TCRP if the stagnation plane profiles in Fig. 14 were to represent the actual experimental profile, was obtained. The methodology outlined in Section 3.5.2 was adopted. The integrated profiles are shown in Fig. 15.

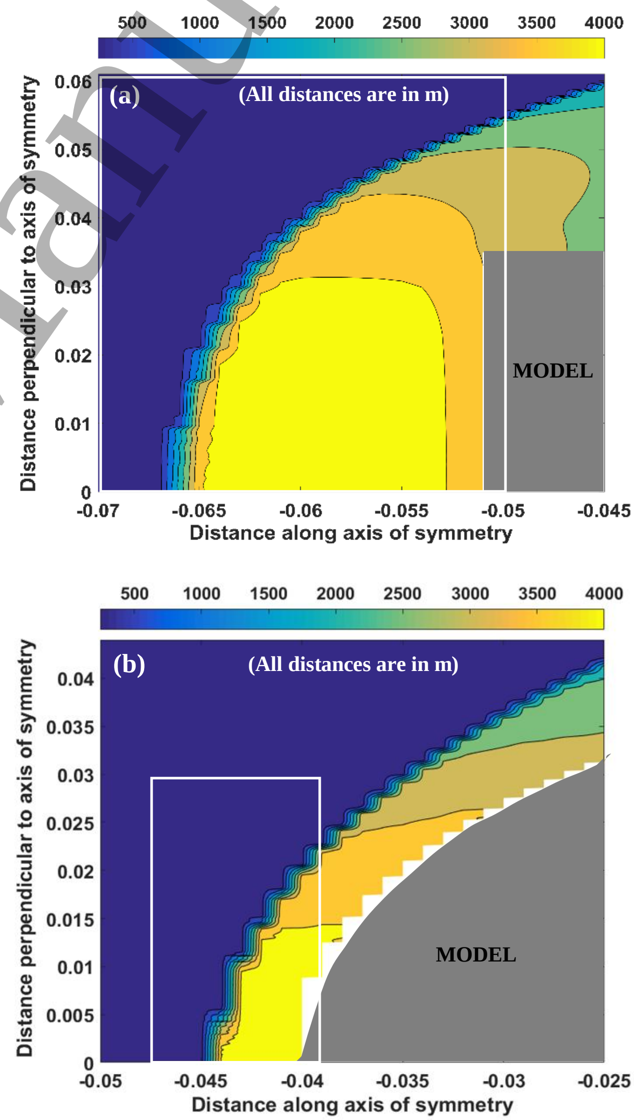

Fig. 15. Integrated 2D temperature contours obtained from simulation, for flow over the (a) Cylinder and (b) Hemisphere.

Along any line-of-sight, the integrated temperature would be close to (but certainly less than) the maximum temperature along that line. This is because the emitted black-body light intensity scales with the 4th power of temperature and majority of the contribution to the path-integrated signal comes from the region with highest temperature. It is for this reason that there are no low temperature (~300 K) regions close to the model wall in Fig. 15. To acknowledge the spatial variation of difference in stagnation plane temperature and integrated temperature, Fig. 16 has been provided. The region of interest is confined only to that marked in Fig. 15 with a white rectangle. The region where wall effects exist (x=-0.04 m, y=0 m) for the hemisphere have been masked.

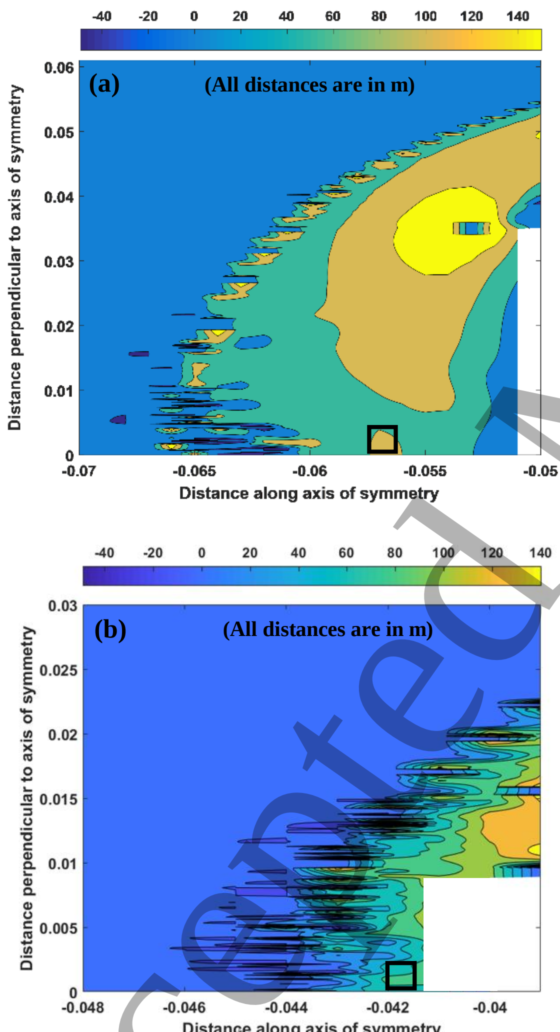

Fig. 16. Spatial distribution of difference between stagnation plane temperature and line-of-sight integrated temperature contours for (a) Cylinder and (b) Hemisphere.

For the cylinder, in the stagnation region at -0.057 m and closest to the axis (marked in Fig. 16), integration effect reduces temperature by about 110 K. For the hemisphere, in the stagnation region at -0.042 m closest to the axis, integration effect reduces temperature by about 76 K.

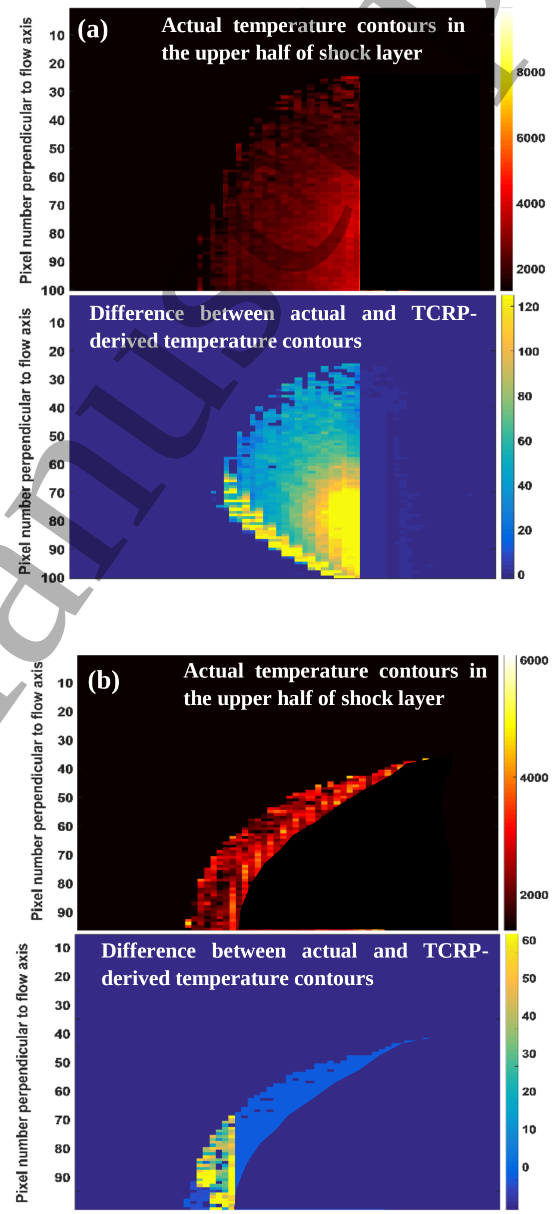

Fig. 17. The actual temperature contours on the stagnation plane (upper half) and difference between actual and TCRP-derived temperature contours (lower half) at t =400 µsec for (a) Cylinder and (b) Hemisphere.

The outlined technique was then employed to obtain the actual temperature contours on the stagnation plane. This was done for each image in the steady test time and actual temperature contours as a function of time was obtained. A comparison between the TCRP-derived temperature and the actual temperature in the stagnation region has been furnished in Table 5. The contours have been compared for t =400 µsec in Fig. 17. In both Fig. 17(a) and 17(b), the upper half is the actual stagnation plane temperature, whereas the lower half is the plot of difference between the actual temperature and the TCRP-derived integrated temperature.

Table 5
Comparison between TCRP- derived and actual temperature in the stagnation region.

Image no.	Time (µsec)	Cylinder temperature (K)		Hemisphere temperature (K)	
		TCRP-derived	Actual	TCRP-derived	Actual
7	300	3590	3685	3283	3341
8	350	3597	3695	3309	3367
9	400	3691	3793	3273	3330
10	450	3676	3775	3313	3371

It may be noted from the table that the actual stagnation plane temperature in case of the cylinder is higher than the TCRP-derived integrated temperature by approximately 100 K consistently across frames during the steady time. As for the hemisphere, it was higher by half that value, about 58 K. This leads to a conclusion that the variation in temperature along the line-of-sight for the hemisphere is lesser compared to that for the cylinder, for reasons discussed in the conclusion section.

It is to be noted that the pressure and temperatures encountered in the shock region are transient. The temperature approaches high values even greater than 3500 K. To our knowledge, there is no easy benchmarking experiment, as in a laminar flame where one can do a controlled calibration experiment at a known temperature and pressure.

5. Uncertainty analysis

One of the major factors contributing to uncertainty in the TCRP technique is the selection of wavelength for source radiance detection. Zhao and Ladommatos [40] mentioned several advantages of the visible spectrum over the infrared, including greater sensitivity of radiation to temperature and lesser intrusion of discrete sharp emissions. TCRP using a color camera ensures working in the visible regime.

The equipment used also presents uncertainty in the results, mainly by way of noise. Svensson *et al.* [41] discussed several noise phenomena for color digital cameras; such as read noise which would be negligible for scientific grade cameras as used in our work, thermally generated noise which was minimized by using a cool camera and addressed by subtracting a dark image, and fixed pattern noise which occurs due to variation in individual pixel sensitivity and was addressed by repeating the camera calibration for different positions of the sensor intercepting light from the calibration lamp. The maximum difference in G/B ratio for the two positions for any temperature (1500 K-4500 K) in the calibration curve was a nominal 0.4% and hence has been neglected. Soot and dust deposition on the optical window of the test section may also add up to the uncertainties in the final result, which is why the window was made to be a part of the calibration set-up.

Apart from these, a sensitivity analysis of TCRP was performed by studying the effect of various parameters on the uncertainty in temperature. These have been elucidated below.

- The effect of choice of focal length (for a fixed exposure time of 49 µsec, same as that used during shock tunnel experiments) on the shot-to-shot and pixel-to-pixel uncertainty in camera signal was determined in a separated calibration experiment. The focal length of the camera lens was varied from 80 mm to 200 mm. It was observed that changing the focal length had negligible effect on signal uncertainty. The shot-to-shot uncertainty and pixel-to-pixel uncertainty were about ±3.8% and ±6.9% respectively, for any chosen focal length.
- Similarly, the effect of choice of exposure time (for a fixed focal length of 80 mm, same as that used during shock tunnel experiments) on the shot-to-shot uncertainty in camera signal was determined. The exposure time of the camera lens was varied from 49 µsec to 1500 µsec. For the exposure time also, it was observed that changing it had negligible effect on signal shot-to-shot uncertainty. The shot-to-shot uncertainty was about ±3.8% for any chosen exposure.
- Using the quantified camera noise (at exposure time of 50 µsec and focal length of 80 mm, same as those used for shock tunnel experiments), an uncertainty analysis was performed based on the calibration between G/B ratio and temperature, to estimate the pixel-to-pixel uncertainty in temperature (in the shock tunnel experiments) due to camera noise for the flow at t=400 µsec. The % uncertainty map of temperature estimated for the cylindrical and hemispherical model are shown below in Fig. 18. It may be noted from the figure that the uncertainty in the shock layer region, where the SNR is high, is very low (maximum of about ±3% and ±6% for the cylinder and hemisphere respectively). However, in regions on the model and in the freestream, the uncertainty rises to as much as ±20% or higher due to poor SNR. These regions are masked in the results.

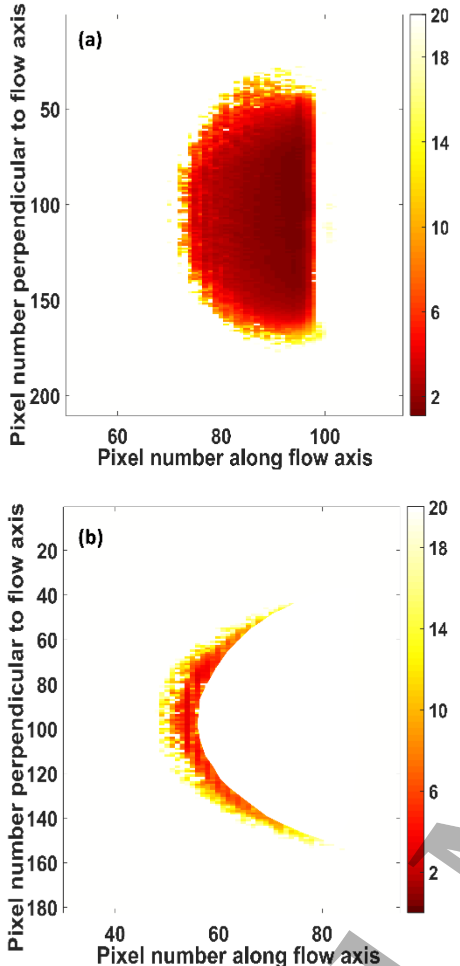

Fig. 18. % Uncertainty in temperature at t =400 μsec due to camera noise for (a) Cylinder and (b) Hemisphere.

To ensure flow repeatability of the shock tunnel, experiments were repeated several times. The run-to-run uncertainty in the driver gas fill pressure was ±1.88% and that for the driven gas was less than ±1.5%. The uncertainty in shock speed measurement was below ±2.5% and that in test time from pitot was about ±4%. The corresponding numbers for the measured stagnation pressure and metal diaphragm bursting pressure were ±2% and ±3% respectively. The stagnation temperature, enthalpy and density from STN had a derived uncertainty of ±1.8%, ±2.2% and ±2.2% respectively. These led to an uncertainty of less than ±2.3% in all free stream quantities, except for Reynolds number/length (±5%).

The color filter array in front of the CMOS sensor of the high-speed color camera has a 'Bayer' pattern which allows intensity measurements in three different channels, namely R, G and B, via an interpolation algorithm known as demosaicing. In that sense, it is a multiple channel pyrometer. The advantage of our design, over some other multi-camera design reported in open literature, such as that by Fu *et al*. [42] is that we need only one camera, so alignment of multiple sensors to match the field of view is not required. Also separate filters are not needed. Their system can be converted to a high-speed one by replacing the CCD cameras with high-speed single channel CMOS cameras.

6. Conclusions

The work was aimed at measuring the temperature in a hypersonic, high-enthalpy dissociating shock layer using two-color ratio pyrometry. The main focus of the paper was to address the problems of time integration and line-of-sight integration of source radiant intensity, which ultimately affects the deduced temperature. The demonstration of the technique in a previous work using a DSLR camera yielded only the temperature values integrated over the entire flow duration. This issue was overcome by using a high speed camera at a frame rate of 20,000 fps to acquire images at an exposure time of 49 μsec and thereby sufficiently sampling the flow having a steady test time of about 260 μsec. The evolution of temperature with time was noted for two different models independently, a flat-faced cylinder and a hemisphere. The steady TCRP-derived temperature for the cylinder in the stagnation region was found to be about 3650 K with an uncertainty of ±3% in the shock layer due to camera noise, whereas for the hemisphere it was about 3300 K (350 K lower) with an uncertainty of ±6%. These values, as explained in the text, were line-of-sight integrated values across the thickness of the shock layer. Detailed CFD simulations were performed in Ansys Fluent to model the actual 3D flow field and an algorithm was developed to obtain the actual temperature in the central (stagnation) plane of the flow from the path-integrated TCRP-derived temperature. The actual temperature in the stagnation region on the vertical plane of symmetry (stagnation plane) for the cylinder was higher by about 100 K than the corresponding TCRP-derived integrated temperature. In case of the hemisphere, the actual temperature was only about 58 K higher. The larger difference in the cylindrical model was because the line-of-sight for the cylinder constituted a larger variation of temperature compared to the case of hemisphere where the transition from the shock region to the free-stream along the line of sight was more sudden.

The effect of time integration was much higher than that of line-of-sight integration on the temperature results. For the cylinder, the time resolved temperature obtained from the high-speed camera during the steady test time was about 14% higher than the time integrated value from the DSLR camera, whereas the actual stagnation plane temperature after accounting for line-of-sight integration was only about 2.76% higher than the integrated one.

The results indicate that a high-speed camera may be readily used as a non-intrusive pyrometer in short duration impulse facilities for accurate shock layer temperature characterization. Also, the measurement technique (TCRP) is simple and easy to implement on a day-to-day basis in shock tunnels.

Acknowledgements

We hereby acknowledge Jeevan, N Kumar and Gangadhar Murthy for providing assistance during the experiments. Technical discussions with Mr Tarandeep Singh have been of immense help to the first author. This work was funded by the Defence Research and Development Organization, India (grant number 0626).

References

[1] Anderson Jr, J.D., 2000. Hypersonic and High Temperature Gas Dynamics (pp. 321-332). AIAA Publications, AIAA, Reston, VA.
[2] Gnoffo, P.A., 1999. Planetary-entry gas dynamics. Annual Review of Fluid Mechanics, 31(1), pp.459-494.
[3] O'Reilly, P.G., Kee, R.J., Fleck, R. and McEntee, P.T., 2001. Two-wire thermocouples: A nonlinear state estimation approach to temperature reconstruction. Review of scientific instruments, 72(8), pp.3449-3457.
[4] Tagawa, M., Kato, K. and Ohta, Y., 2005. Response compensation of fine-wire temperature sensors. Review of Scientific Instruments, 76(9), p.094904.
[5] Brohez, S., Delvosalle, C. and Marlair, G., 2004. A two-thermocouples probe for radiation corrections of measured temperatures in compartment fires. Fire Safety Journal, 39(5), pp.399-411.
[6] Mitani, T., Takahashi, M., Tomioka, S., Hiraiwa, T. and Tani, K., 1999. Analyses and application of gas sampling to scramjet engine testing. Journal of Propulsion and Power, 15(4), pp.572-577.
[7] Struk, P., Dietrich, D., Valentine, R. and Feier, I., 2003, February. Comparisons of gas-phase temperature measurements in a flame using thin-filament pyrometry and thermocouples. In 41st Aerospace Sciences Meeting and Exhibit (p. 853).
[8] Park, C.S., Newfield, M.E., Fletcher, D.G., G-ograve, T., k-atilde and en, 1999. Spectroscopic measurements of shock-layer flows in an arcjet facility. Journal of thermophysics and heat transfer, 13(1), pp.60-67.
[9] Lee, M.P., McMillin, B.K. and Hanson, R.K., 1993. Temperature measurements in gases by use of planar laser-induced fluorescence imaging of NO. Applied Optics, 32(27), pp.5379-5396.
[10] Palma, P.C., Mallinson, S.G., O', S.B., Byrne, Danehy, P.M. and Hillier, R., 2000. Temperature measurements in a hypersonic boundary layer using planar laser-induced fluorescence. AIAA journal, 38(9), pp.1769-1772.
[11] Gerardi, C., Buongiorno, J., Hu, L.W. and McKrell, T., 2010. Study of bubble growth in water pool boiling through synchronized, infrared thermometry and high-speed video. International Journal of Heat and Mass Transfer, 53(19-20), pp.4185-4192.
[12] Stenberg, J., Frederick, W.J., Boström, S., Hernberg, R. and Hupa, M., 1996. Pyrometric temperature measurement method and apparatus for measuring particle temperatures in hot furnaces: Application to reacting black liquor. Review of scientific instruments, 67(5), pp.1976-1984.
[13] Kappagantula, K., Crane, C. and Pantoya, M., 2013. Determination of the spatial temperature distribution from combustion products: a diagnostic study. Review of Scientific Instruments, 84(10), p.104902.
[14] Cignoli, F., De Iuliis, S., Manta, V. and Zizak, G., 2001. Two-dimensional two-wavelength emission technique for soot diagnostics. Applied Optics, 40(30), pp.5370-5378.
[15] Weismiller, M.R., Lee, J.G. and Yetter, R.A., 2011. Temperature measurements of Al containing nano-thermite reactions using multi-wavelength pyrometry. Proceedings of the Combustion Institute, 33(2), pp.1933-1940.
[16] Zander, F., 2016. Surface temperature measurements in hypersonic testing using digital single-lens reflex cameras. Journal of Thermophysics and Heat Transfer, 30(4), pp.919-925.
[17] Fu, T., Cheng, X., Shi, C., Zhong, M., Liu, T. and Zheng, X., 2006. The set-up of a vision pyrometer. Measurement Science and Technology, 17(4), p.659.
[18] Densmore, J.M., Homan, B.E., Biss, M.M. and McNesby, K.L., 2011. High-speed two-camera imaging pyrometer for mapping fireball temperatures. Applied optics, 50(33), pp.6267-6271.
[19] Deep, S., Krishna, Y. and Jagadeesh, G., 2017. Temperature characterization of a radiating gas layer using digital-single-lens-reflex-camera-based two-color ratio pyrometry. Applied optics, 56(30), pp.8492-8500.
[20] Lu, H., Ip, L.T., Mackrory, A., Werrett, L., Scott, J., Tree, D. and Baxter, L., 2009. Particle surface temperature measurements with multicolor band pyrometry. AIChE journal, 55(1), pp.243-255.
[21] MacDonald, M.E., Jacobs, C.M., Laux, C.O., Zander, F. and Morgan, R.G., 2014. Measurements of air plasma/ablator interactions in an inductively coupled plasma torch. Journal of Thermophysics and Heat Transfer, 29(1), pp.12-23.
[22] Schuck, D., 2013. Fiber-based emission spectroscopy on a cylindrical body in the T-ADFA hypersonic shock tunnel. In 51st AIAA Aerospace Sciences Meeting including the New Horizons Forum and Aerospace Exposition (p. 127).
[23] Schott, T., Munk, M., Herring, G., Grinstead, J. and Prabhu, D.K., 2010, January. Fiber-based measurement of bow-shock spectra for reentry flight testing. In 48th AIAA Aerospace Sciences Meeting Including the New Horizons Forum and Aerospace Exposition (p. 301).
[24] Payri, F., Pastor, J.V., García, J.M. and Pastor, J.M., 2007. Contribution to the application of two-colour imaging to diesel combustion. Measurement science and technology, 18(8), p.2579.
[25] Stalker, R.J., 1966. The free-piston shock tube. The Aeronautical Quarterly, 17(4), pp.351-370.
[26] Jayaram, V., 2009. Experimental investigations of surface interactions of shock heated gases on high temperature materials using high enthalpy shock tubes (Doctoral dissertation, G21519).
[27] Kumar, C.S., 2017. Experimental Investigation of Aerodynamic Interference Heating Due to Protuberances on Flat Plates and Cones Facing Hypersonic Flows (Doctoral dissertation, G26271).

[28] Zucker, R.D. and Biblarz, O., 2002. Fundamentals of gas dynamics. John Wiley & Sons.
[29] Tanno, H., Itoh, K., Komuro, T. and Sato, K., 2000. Experimental study on the tuned operation of a free piston driver. Shock Waves, 10(1), pp.1-7.
[30] Krek, R.M. and Jacobs, P.A., 1993. STN, shock tube and nozzle calculations for equilibrium air. Department of Mechanical Engineering, The University of Queensland.
[31] Gunturk, B.K., Glotzbach, J., Altunbasak, Y., Schafer, R.W. and Mersereau, R.M., 2005. Demosaicking: color filter array interpolation. IEEE Signal processing magazine, 22(1), pp.44-54.
[32] Liepmann, H.W., Narasimha, R. and Chahine, M.T., 1962. Structure of a plane shock layer. The Physics of Fluids, 5(11), pp.1313-1324.
[33] Brown, J., 2002. Turbulence model validation for hypersonic flows. In 8th AIAA/ASME Joint Thermophysics and Heat Transfer Conference (p. 3308).
[34]https://www.sharcnet.ca/Software/Fluent6/html/ug/node487.htm
[35]http://combustion.berkeley.edu/gri_mech/data/thermo_table.html
[36]http://www.afs.enea.it/project/neptunius/docs/fluent/html/th/node129.htm
[37] http://kinetics.nist.gov/kinetics/KineticsSearchForm.jsp
[38] Kempema, N.J. and Long, M.B., 2018. Effect of soot self-absorption on color-ratio pyrometry in laminar coflow diffusion flames. Optics letters, 43(5), pp.1103-1106.
[39] Bayer, B.E., 1976. Color imaging array. US patent 3,971,065.
[40] Zhao, H. and Ladommatos, N., 1998. Optical diagnostics for soot and temperature measurement in diesel engines. Progress in Energy and Combustion Science, 24(3), pp.221-255.
[41] Svensson, K.I., Mackrory, A.J., Richards, M.J. and Tree, D.R., 2005. Calibration of an RGB, CCD Camera and Interpretation of its Two-Color Images for KL and Temperature (No. 2005-01-0648). SAE Technical Paper.
[42] Fu, T., Liu, J. and Tian, J., 2017. VIS-NIR multispectral synchronous imaging pyrometer for high-temperature measurements. Review of Scientific Instruments, 88(6), p.064902.